Structure
Article

Extended Polypeptide Linkers Establish the Spatial Architecture of a Pyruvate Dehydrogenase Multienzyme Complex

Jeffrey S. Lengyel,[1,2] Katherine M. Stott,[2] Xiongwu Wu,[3] Bernard R. Brooks,[3] Andrea Balbo,[4] Peter Schuck,[4] Richard N. Perham,[2] Sriram Subramaniam,[1] and Jacqueline L.S. Milne[1,*]
[1]Laboratory of Cell Biology, National Cancer Institute, NIH, Bethesda, MD 20892, USA
[2]Department of Biochemistry, University of Cambridge, Cambridge CB2 1GA, UK
[3]Laboratory of Computational Biology, National Heart Lung and Blood Institute, NIH, Bethesda, MD 20892, USA
[4]Protein Biophysics Resource, National Institute of Biomedical Imaging and Bioengineering, NIH, Bethesda, MD 20892, USA
*Correspondence: jmilne@nih.gov
DOI 10.1016/j.str.2007.10.017

SUMMARY

Icosahedral pyruvate dehydrogenase (PDH) enzyme complexes are molecular machines consisting of a central E2 core decorated by a shell of peripheral enzymes (E1 and E3) found localized at a distance of ~75–90 Å from the core. Using a combination of biochemical, biophysical, and cryo-electron microscopic techniques, we show here that the gap between the E2 core and the shell of peripheral enzymes is maintained by the flexible but extended conformation adopted by 60 linker polypeptides that radiate outwards from the inner E2 core, irrespective of the E1 or E3 occupancy. The constancy of the gap is thus not due to protein-protein interactions in the outer protein shell. The extended nature of the E2 inner-linker regions thereby creates the restricted annular space in which the lipoyl domains of E2 that carry catalytic intermediates shuttle between E1, E2, and E3 active sites, while their conformational flexibility facilitates productive encounters.

INTRODUCTION

Pyruvate dehydrogenase (PDH) complexes are multifunctional enzymes that efficiently coordinate catalysis between three spatially separated active sites by using a swinging arm covalently attached to one of the constituent enzymes to transport reaction intermediates between them. PDH complexes can be based on octahedral or icosahedral symmetry, but both contain three essential enzymes that are required for the catalytic cycle: a thiamine-dependent pyruvate decarboxylase (E1), a dihydrolipoyl acetyltransferase (E2), and a flavoprotein dihydrolipoyl dehydrogenase (E3) (Reed and Hackert, 1990; Perham, 1991, 2000). Abnormal function or diminished activity of PDH complexes has been implicated in various metabolic disorders (Patel and Harris, 1995; Yeaman et al., 2000; Nellis and Danner, 2001), neurodegenerative diseases (Bubber et al., 2005), aging (Tahara et al., 2007), and cancer (Koukourakis et al., 2005; Kim et al., 2006). Mammalian PDH complexes are located within mitochondria and are a little more elaborate than their bacterial counterparts, possessing an additional E3-binding protein as well as regulatory kinases and phosphatases (Perham, 2000; Ciszak et al., 2006).

Extensive biochemical analysis, X-ray crystallographic, and NMR spectroscopic studies have provided detailed descriptions of individual components in the PDH complex, in particular that from *Bacillus stearothermophilus*, including the active site chemistries of the four reactions mediated by them (Perham, 1991, 2000; Frank et al., 2004; Fries et al., 2007), specific interactions of high affinity between the constituent polypeptides (Lessard and Perham, 1995), and the structures of the E1 $\alpha_2\beta_2$ tetramer, the E3 homodimer, and the subdomains of the E2 chain (Mande et al., 1996; Izard et al., 1999; Perham 2000; Frank et al., 2005). Similar studies have been reported for the PDH complex of *Escherichia coli* (Reed and Hackert, 1990; Arjunan et al., 2002; Kale et al., 2007, and references therein) and related 2-oxo acid dehydrogenase complexes from other sources (Perham, 2000). Cryo-electron microscopic analysis of bacterial (Wagenknecht et al., 1990, 1992; Milne et al., 2002, 2006; Murphy and Jensen, 2005) and eukaryotic (Wagenknecht et al., 1991; Zhou et al., 2001; Gu et al., 2003) PDH complexes has begun to reveal fascinating glimpses of the architecture of the assembled complexes, although how the spatial arrangement of their constituent enzymes is established and maintained remains unresolved.

The *B. stearothermophilus* PDH complex is a well-characterized prototype of those based on icosahedral symmetry. It is assembled around an E2 core of 60 E2 polypeptide chains, each of which contains a C-terminal 28 kDa catalytic domain, a central 4 kDa peripheral subunit-binding domain (PSBD), and an N-terminal 9 kDa lipoyl domain (to which the swinging arm, a lipoyl group, is covalently attached), connected respectively by a long inner-linker region and an even longer outer-linker region thought to be largely flexible in nature (Reed and Hackert, 1990; Perham, 1991; Green et al., 1992; Fries et al., 2007). It is the lipoyl domain that has to migrate between the E1, E2, and E3 active sites for each turn of the catalytic cycle. To generate the native *B. stearothermophilus* PDH complex, 60 copies of the catalytic domain of the E2 chain self-assemble to form an icosahedral structure (Izard et al., 1999), and between 42–48 copies of the E1 $\alpha_2\beta_2$ tetramer and 6–12 copies of the E3 homodimer bind tightly but mutually exclusively to the 60 PSBDs that lie around the outside of the E2 core (Lessard and Perham, 1995; Domingo et al., 1999).

Recent cryo-electron microscope analysis of recombinant *B. stearothermophilus* E1E2 and E2E3 subcomplexes in which either 60 E1 heterotetramers or 60 E3 homodimers occupy all 60 PSBD binding sites have provided more detailed insights into the three-dimensional (3D) organization of icosahedral PDH complexes. The E1 or E3 components are observed to form an outer shell with an annular gap of ~75–90 Å between the outer surface of the E2 core and the regions at each 3-fold vertex where the inner linker joins the peripheral subunit binding domain to which E1 and E3 bind (Milne et al., 2002, 2006). The creation of this annular space or gap suggests an improved means of substrate channeling, both by restricting the volume that the lipoyl domains of the E2 core must sweep through in cycling between the E1, E2, and E3 active sites and by lessening potentially deleterious interactions of a lipoyl domain with E1 or E3 as it shuttles back and forth between the E2 core and the outer layer of E1 and E3 enzymes.

Several potential ways of maintaining this unexpected architecture of the overall PDH complex can be envisaged. One possibility is that protein-protein interactions among E1 components and/or E3 components might help position the outer shell enzymes above the inner E2 core (Milne et al., 2002, 2006). These interactions could be simply steric in nature or involve some multimerization of enzymes in the outer shell. An alternative scenario is that the inner-linker region is itself sufficiently rigid and extended to maintain the gap between the inner E2 core and the outer enzyme shell. However, in contrast with the extended by highly flexible outer-linker regions in the E2 chains of both *E. coli* (Radford et al., 1989; Green et al., 1992) and *B. stearothermophilus* (Fries et al., 2007) PDH complexes, relatively little is known about the properties of the inner linker that might shed light on the latter possibility.

Here, we describe the first, to our knowledge, detailed biophysical characterization of a synthetic peptide representing a PDH inner-linker region to determine what, if any, structural elements are present. We show that the peptide remains monomeric and adopts a highly flexible but extended conformation in solution. To our knowledge, our work is the first to quantify the population of α and β structures in one of these linkers residue by residue using secondary chemical shifts (13C being the most reliable indicator) and reveals a true preference over all residues for β structures despite the highly flexible nature of the peptide. We also present cryo-electron microscopic analysis of PDH complexes consisting of E2 cores decorated partially or fully with E1 heterotetramers or E3 homodimers, which reveals that the positioning of the peripheral enzymes in the complex is independent of the occupancy of E1 or E3. The unique spatial geometry of the PDH complex is thus dictated primarily by the extended nature of the inner-linker region of the E2 chain, and not by protein-protein interactions in the outer shell. Further, we gain insights into the local disorder in the arrangement of enzymes in the outer shell and speculate on how this dynamic architecture would promote efficient catalysis.

RESULTS

Secondary Structure and Quaternary Structure of the Inner-Linker Peptide

To span a gap of 90 Å between the shell of E1 and the inner E2 core requires a segment of polypeptide chain of at least 30 amino acid residues (3.5 Å per residue fully extended). Based on the structures of the PSBD (Kalia et al., 1993; Allen et al., 2005) and the acetyltransferase domain (Izard et al., 1999), we have proposed that the linker region in *B. stearothermophilus* E2 most likely begins around residue Ala167, which is at the C-terminal end of the PSBD, and extends to around residue Ser203, which is at the N-terminal end of the structure of the acetyltransferase domain (Milne et al., 2002). To investigate the secondary structure and other biophysical properties of this E2 inner linker, we synthesized a 37 residue peptide with the same amino acid sequence, AGGAKPAPAAAEEKAAPAAAKPATTEGEFPETR EKMS. The peptide was applied to a Superdex 75 gel filtration column with the SMART system calibrated with E1 (Lessard and Perham, 1994), the E2 lipoyl domain (Dardel et al., 1993), and thiamine diphosphate. The peptide eluted in a position corresponding to an apparent molecular mass close to the theoretical value of ~3.7 kDa (Figure 1A), indicating that it is monomeric. The circular dichroism spectrum (180 nm to 175 nm) of the linker peptide (Figure 1B) is consistent with it adopting the conformation of a random coil, exhibiting a minimum at ~197 nm and a maximum at ~219 nm and lacking any noticeable signatures that would suggest the presence of persistent α-helical or β sheet secondary structural elements.

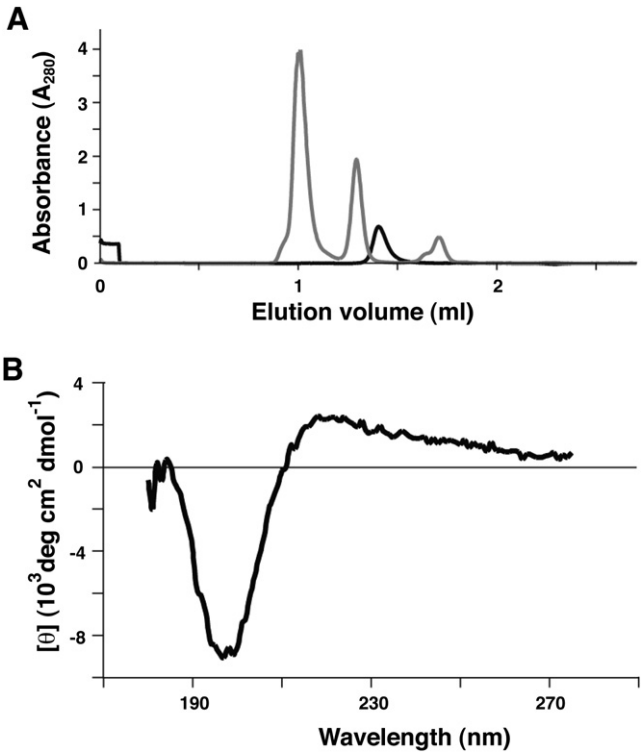

Figure 1. Characterization of the Inner-Linker Peptide
(A) Gel filtration chromatography of purified peptide (black line) calibrated against a standard (gray line) of E1 (~150 kDa, left peak), lipoyl domain (~10 kDa, central peak), and thiamine diphosphate (right peak).
(B) Circular dichroism spectrum of the peptide.

NMR Analysis of the Structure and Dynamics of the Inner-Linker Peptide

Two-dimensional NMR spectroscopy was carried out with ^{1}H-^{1}H TOCSY (total correlation spectroscopy), ^{1}H-^{1}H NOESY (nuclear

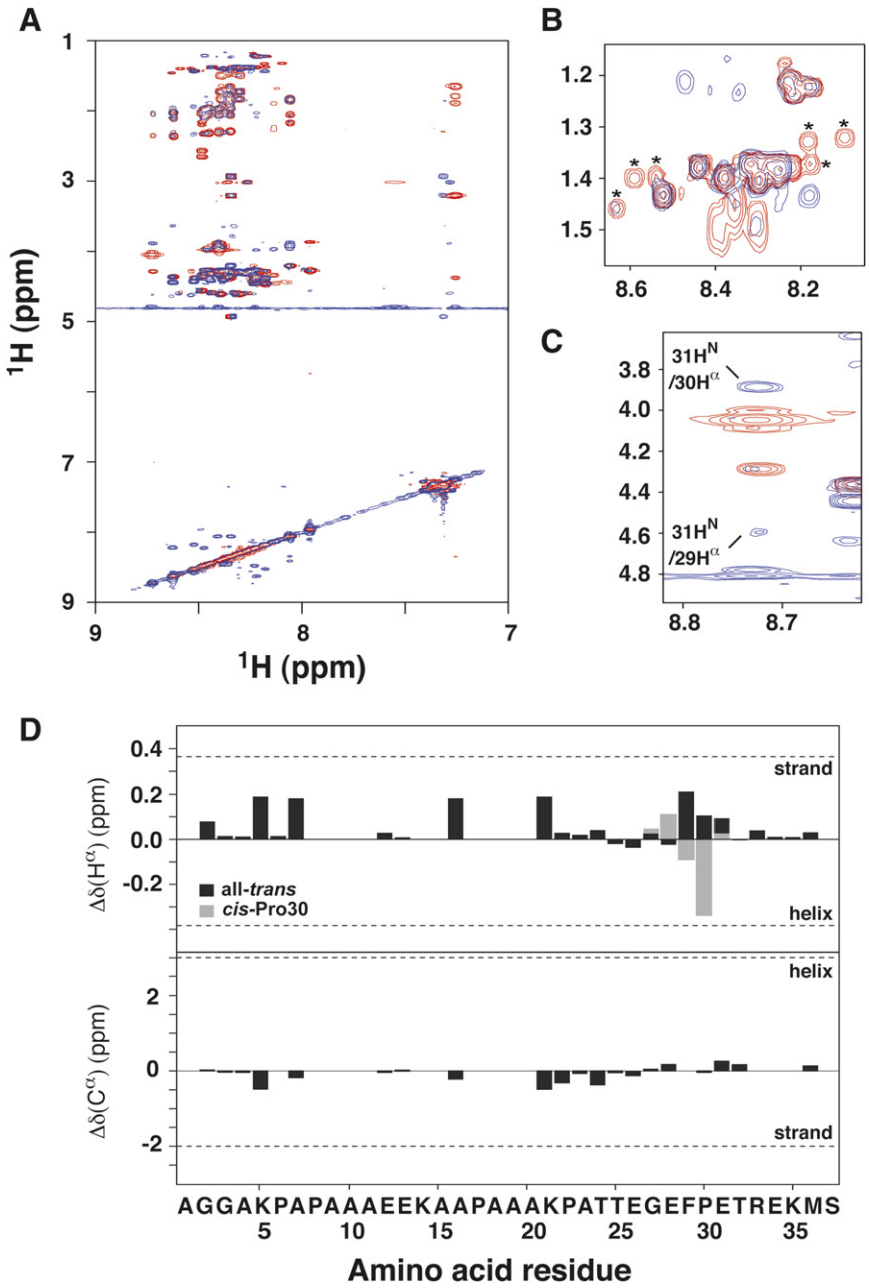

Figure 2. 2D NMR Spectroscopy of the Inner-Linker Peptide

(A) 7.0–9.0 ppm region of ^{1}H-^{1}H NOESY (blue) and TOCSY (red) spectra of the inner-linker peptide. The peptide is monomeric and largely flexible (see text for details).

(B) TOCSY crosspeaks revealing the presence of *cis*-Pro isomers at ~8% levels are indicated by asterisks.

(C) NOESY crosspeaks revealing the presence of a *cis* isomer of Pro30, present at a ~20% level and populating a type-VI turn; a weak medium-range $d_{\alpha N}(i,i+2)$ NOE is shown that connects residues 29 and 31 across the turn.

(D) Deviations of H$^\alpha$ and C$^\alpha$ chemical shifts from random-coil values, corrected for sequence context (Schwarzinger et al., 2001). Dotted horizontal lines mark average deviations seen in stable α helices and β strands (Wishart et al., 1991). No regions of large and consistent deviations were seen, indicating the lack of stable secondary structure in the all-*trans* form; however, slight preferences for β/extended structures may be inferred for residues 2–24 in the conformational ensemble (see text). The residue *cis*-Pro30 populates a type-VI turn, and the H$^\alpha$ displays a characteristic large upfield shift (Yao et al., 1994).

Överhauser effect spectroscopy), and ^{1}H-^{13}C HSQC (heteronuclear single quantum correlation), recorded with a large number of transients to compensate for the low levels of ^{13}C present (1.07%) at natural abundance. The 7.0–9.0 ppm regions of the NOESY and TOCSY spectra are shown in Figure 2A. In general, the peaks are sharp and poorly dispersed, indicating that the peptide is monomeric and flexible.

Of the 37 residues in the peptide, 26 could be assigned unambiguously. Of the 11 remaining residues, 10 (8–11, 14–15, and 17–20) could only be given ambiguous assignments, owing to extensive resonance overlap arising from the lack of sequence variation in the Ala/Pro-rich N-terminal half of the peptide. ^{13}C resonances could be assigned for 25 residues. The NOESY spectrum revealed many sequential NOE crosspeaks. For residues 2–24, $d_{\alpha N}(i,i+1)$ and $d_{\beta N}(i,i+1)$ but no $d_{NN}(i,i+1)$ crosspeaks were observed. For residues 25–37, the $d_{\alpha N}(i,i+1)$, $d_{\beta N}(i,i+1)$, and $d_{NN}(i,i+1)$ were generally of comparable intensity. This suggests that, although flexible, the peptide is populating both α-like and β-like structures in the C-terminal region but is preferentially populating β-like structures in the N-terminal region (Wüthrich, 1986).

The sequence contains five proline residues: ^{5}K**P**A^7, ^{7}A**P**A^9, ^{16}A**P**A^{18}, ^{21}K**P**A^{23}, and ^{29}F**P**E^{31}. The chemical shifts of these residues indicated that the Xaa-Pro peptide bonds were all in the *trans* conformation (Schwarzinger et al., 2000). Evidence of alternate conformers was seen in the form of weak peaks in the spectra with chemical shifts characteristic of *cis*-Pro; these were most conspicuous in the region corresponding to the alanine H^N/(H$^\beta$)$_3$ crosspeaks (Figure 2B). With the exception of the conformer corresponding to *cis*-Pro30 (see below), these could not be assigned to specific sequences. However, the expected number of Xaa-*cis*-Pro-Ala and Ala-*cis*-Pro were seen. Based on the mean volumes of alanine H^N/(H$^\beta$)$_3$ NOESY crosspeaks, the average percentage of the *cis* form for proline residues 6, 8, 17, and 22 was 8.25% of the total.

This is in contrast to the conformer seen corresponding to *cis*-Pro30 (^{29}F**P**E^{31}), which could be unambiguously identified, and corresponds to ~20% of the total as judged by crosspeak intensities. Two sets of peaks, corresponding to the *cis* and the *trans*

isomer, were seen in the stretch Gly27-Thr32, which diverge in chemical shift significantly in the range Glu28-Glu31. The only medium-range NOE observed in the spectrum (Figure 2C) was a weak $d_{\alpha N}(i,i+2)$ connection between Phe29 and Glu31 in the *cis*-Pro30 conformer. This indicates that the sequence ^{29}FPET^{32} populates a type-VI turn, typical of sequences in which aromatic residues flank proline and stabilize the turn through ring stacking (Yao et al., 1994). This is further supported by secondary chemical shifts, e.g., the H^{α} resonance of *cis*-Pro30, which shows a significant upfield shift (Figures 2C and 2D).

With the exception of Gly2 and Ser37 at the N and C termini, and Glu31 in the *cis*-Pro30 conformer (see above), all H^{N} resonances lie in the range 8.1–8.6 ppm expected for a random coil (Schwarzinger et al., 2000). This observation is consistent with the narrow line widths and the lack of medium-range NOE connectivities, which taken together strongly suggest that the all-*trans* form of the peptide is unstructured and flexible. However, "random-coil" chemical shifts are assumed to be the result of temporal averaging (Wishart et al., 1991); any preference for α helix or β strand/extended structure is reflected in significant and consistent deviations from random-coil shifts that persist over several sequential residues, particularly for H^{α} and C^{α}. Small deviations were seen along the entire sequence (Figure 2C), with no long tracts of large and consistent deviations indicative of stable α helix or β strand. However, comparing the graphs for both nuclei, there is a consistent preference for β strand/extended structure in the Ala/Pro-rich N-terminal section (residues 2–24), consistent with the lack of $d_{NN}(i,i+1)$ crosspeaks in this region. Residues preceding proline display the largest deviations; the H^{α} deviations for Xaa-Pro may be overemphasized since the original study used the peptide Ac-GGPGG-NH_2, which adopts a local structure not possible for amino acids with bulkier side chains (Wishart et al., 1995). However, even taking this into account, the preference for β strand/extended structure is clear, although no evidence for any persistent α-helical or β strand is observed, consistent with the inferences drawn above from circular dichroism spectroscopy.

Analytical Ultracentrifugation of the Inner-Linker Peptide

Sedimentation velocity analytical ultracentrifugation was undertaken on the peptide to determine its hydrodynamic radius. The best-fit molecular mass of the peptide was 3.62 kDa, close to its calculated mass of 3.64 kDa. The peptide migrated as a homogeneous population, confirming that it is monomeric in solution (Figure 3). The sedimentation coefficient, $s_{20,w}$, of the peptide was found to be 0.585 S ± 0.002 S, which corresponds to a hydrodynamic frictional ratio of 1.50 and is suggestive of an asymmetric molecule. Based on the predicted maximal hydration of 0.55 g/g (from consideration of the amino acid composition and the tables by Kuntz [1971]), this can be modeled hydrodynamically as a prolate ellipsoid with major and minor axis dimensions of 2a = 70 Å and 2b = 15 Å, respectively. It is difficult to assign precise molecular dimensions to the peptide by using hydrodynamic shape estimation because its level of hydration is unknown. However, if less hydration is assumed, this would only further increase the value of the major axis (up to 89 Å in the extreme of no hydration). Thus, the hydrodynamic data suggest that the peptide adopts a substantially elongated shape in solution with an apparent length of 70 Å or more.

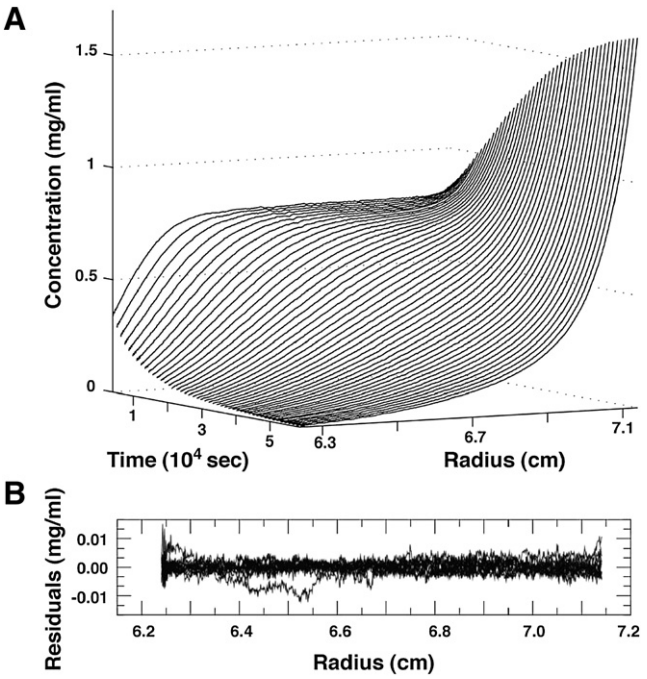

Figure 3. Analytical Ultracentrifugation of the Inner-Linker Peptide

(A) Evolution of the experimental concentration distributions during the sedimentation experiment of the peptide at 60,000 rpm, as detected with the Rayleigh interference optical data acquisition (after subtraction of the baseline signal offsets).

(B) Residuals of the single species Lamm equation fit, which was part of a global analysis of several data sets at different loading concentrations and acquired with different optical systems.

Electron Microscopic Analysis of PDH Subcomplexes in Various Stages of Assembly

The biophysical and spectroscopic studies with the isolated peptide described above are consistent with it adopting an extended conformation. This in turn suggests that the annular gap in assembled PDH complexes may be dictated primarily by properties of the inner-linker region of the E2 chain. To test this hypothesis, we prepared a series of E1E2 and E2E3 subcomplexes that contained E2 cores decorated with E1 or E3 enzymes at predicted average occupancies of 17%, 33%, 67%, and 100%. The goal of these experiments was to image the locations of outer shell enzymes in individual subcomplexes and determine whether the radial distances were influenced by the level of occupancy of the outer shell.

The polypeptide chain ratios of the E1E2 and E2E3 subcomplexes were analyzed by SDS-polyacrylamide gel electrophoresis (Figure 4). Similar amounts of E2 are evident in each lane. The amounts of the 43 kDa and 36 kDa bands, corresponding to the E1α subunit and E1β subunit, respectively, increased as the E1 occupancy of the E1E2 subcomplexes rose to its expected maximum level of 100% (Figure 4A). Similar results were seen for the E2E3 subcomplexes, where the intensity of the 50 kDa band corresponding to the E3 monomer increased as the assembly progressed toward 100% occupancy (Figure 4B). Densitometric

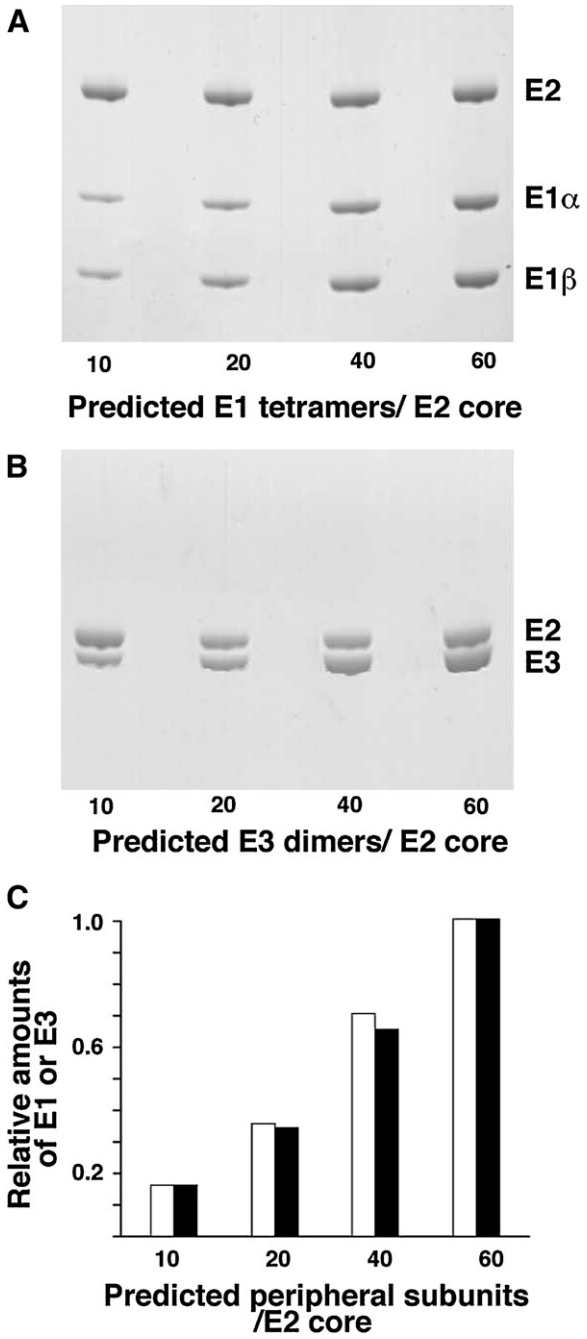

Figure 4. SDS-Polyacrylamide Gel Electrophoresis of PDH Subcomplexes

Purified E1E2 (A) and E2E3 (B) complexes with the indicated E1or E3 occupancies were loaded onto gels to have comparable amounts of E2, to facilitate normalization during densitometry. (C) Relative amounts of E1 (white bars) or E3 peripheral subunits (black bars) per E2 subunit were measured in each complex by densitometry of the Coomassie-blue-stained gels, based on setting occupancy of the complex with 60 E1 or 60 E3 enzymes bound to the E2 core to a value of 1.0.

analysis of the Coomassie-stained gels confirmed that the E1:E2 or E3:E2 chain ratios were close to the predicted occupancies of E1 and E3 in the variously assembled subcomplexes (Figure 4C).

Cryo-electron microscopic projection images (Figure 5) of the lowest occupancy E1E2 and E2E3 subcomplexes revealed the characteristic icosahedral shape of the 1.8 MDa E2 acetyltransferase core assembly surrounded by a few scattered dense particles, apparently randomly distributed, which had dimensions consistent with the predicted sizes of the E1 heterotetramer (Frank et al., 2005) or E3 homodimer (Mande et al., 1996). As the 60 PSBDs per E2 core became increasingly occupied by E1 heterotetramers or E3 homodimers, the E2 core became correspondingly less visible, shadowed by an increasing number of peripheral densities (Figure 5). Rotational averages of several hundred well-separated projection images of each type of E1E2 subcomplex showed that the amplitude of the inner ring of E2 density remained constant, with a radius of 110 Å, which is consistent with its known size (Izard et al., 1999). The radius of the outermost density surface, corresponding to the E1 enzyme densities, remained relatively constant at ~240 Å in all of the subcomplexes, the same as that of the fully assembled E1E2 subcomplex in 3D cryo-electron microscopic reconstructions (Milne et al., 2002). As expected, the density of the peripheral ring increased progressively as a function of E1 occupancy level. Similar results were obtained for the series of E2E3 subcomplexes, except that the radius of the outermost ring of density was about 228 Å, i.e., ~10–15 Å smaller than the radius of the E1 protein shell in the E1E2 subcomplexes. This too is consistent with the size of the 3D reconstruction of the fully assembled E2E3 subcomplex (Milne et al., 2006).

The average size of the E1E2 and E2E3 radial density distributions is illustrated in Figure 6. The E1E2 radial plots indicate that the distance from the center of the E2 density to the center of the E1 density is 94 Å, 98 Å, 110 Å, and 104 Å for the subcomplexes with E1 occupancies of 17%, 33%, 66%, and 100%, respectively. The mean gap distance (measured peak to peak) for the E1E2 complexes is 102 Å ± 7 Å. Note that since projection images include contributions to the density from all regions of the complex, this is a different and complementary measure of the rotationally averaged gap distance, in contrast to the 75–90 Å value measured in 3D for the distance between the outer surface of the E2 core and the regions at each 3-fold vertex where the inner linker joins the PSBD. Similarly, the E2E3 radial plots exhibited center-to-center distances between the densities attributed to E2 and E3 of 85 Å, 91 Å, 96 Å, and 98 Å for the 17%, 33%, 66%, and 100% E3-occupancy subcomplexes, respectively. The mean gap distance (measured peak to peak) for the E2E3 complexes is thus 93 Å ± 6 Å. These results strongly suggest that the gap between the inner core and the outer shell is largely independent of the level of occupancy of enzymes in the outer shell and confirm the finding that the annular gap of E1E2 subcomplexes is slightly larger than that of E2E3 subcomplexes (Milne et al., 2002, 2006).

Cryo-Electron Tomography of Individual E1E2 Subcomplexes

Since the radial density profiles derived above arise from averaging projection images from several PDH subcomplexes, it is formally possible that there is local clustering in each of the partial occupancy complexes that leads to the observed gap. Further, determination of the radial distance in projection could also be subject to systematic artifacts in estimating the separation

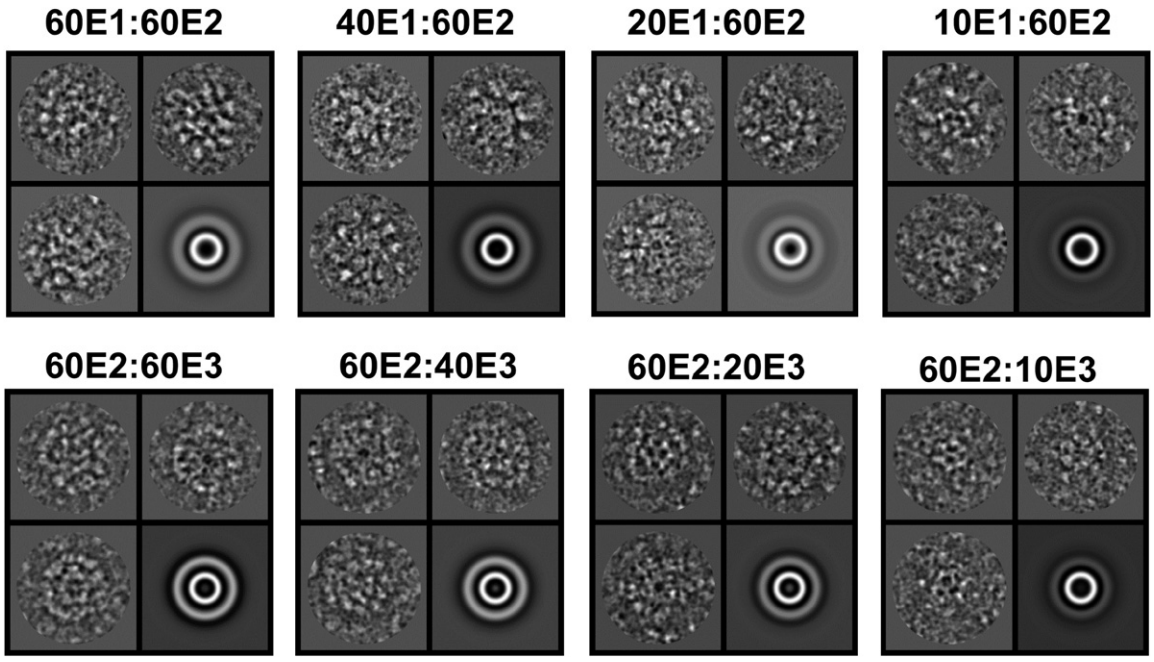

Figure 5. Cryo-Electron Microscopy of PDH Subcomplexes

Representative molecular images of each set of E1E2 (top panels) or E2E3 (lower panels) subcomplexes were collected as described in Experimental Procedures. The bottom right panel shown for each complex is a rotational average derived from 482 10E1:60E2, 354 20E1:60E2, 716 40E1:60E2, 613 60E1:60E2, and 577 10E3:60E2, 435 20E3:60E2, 696 40E3:60E2, or 566 60E3:60E2, respectively.

between the inner core and the outer shell. To confirm unambiguously the role of the inner linker as the primary structural determinant underlying the annular gap, we employed cryo-electron tomography to visualize individual E1 peripheral enzymes in E1E2 subcomplexes.

Using samples identical to those used for the projection imaging in Figure 5, a series of tilted images, typically spanning an angular range from −65° to +65°, were recorded from frozen hydrated specimens of E1E2 and E2E3 subcomplexes at total doses of <60 electrons/Å^2. Automated reconstruction algorithms were used to convert the images to tomograms, which reveal the 3D shapes of the individual complexes. A representative example of a selected reconstruction from a typical full-occupancy E1E2 PDH subcomplex is shown in Figure 7A. The densities corresponding to the E2 core as well as the outer shell enzymes are clearly visible. Despite the extremely low signal-to-noise ratio in this image of single complexes, as compared with the 3D maps obtained by averaging thousands of images and imposing icosahedral symmetry, the overall architecture of the annular gap could be readily visualized within a single PDH complex. Although the densities of individual E1 enzymes are too noisy to dock the atomic coordinates reliably, the center of mass of each of the peripheral densities could be aligned by means of core-weighted search procedures (Wu et al., 2003) by using, as a template, the crystallographically determined structure of the E1 heterotetramer (Frank et al., 2005) filtered to 30 Å resolution. The resulting fit (Figure 7C) provides useful representations of the individual densities in terms of the spatial distribution of the E1 molecules relative to the core and relative to each other, even though the precise orientation of each of the E1 enzymes in the complex is not accurately determined. The results of a similar analysis carried out with low-occupancy E1E2 subcomplexes are shown in Figures 7B and 7D, respectively. As in the case of the full-occupancy subcomplexes, the densities corresponding to the core and the outer shell can be easily identified.

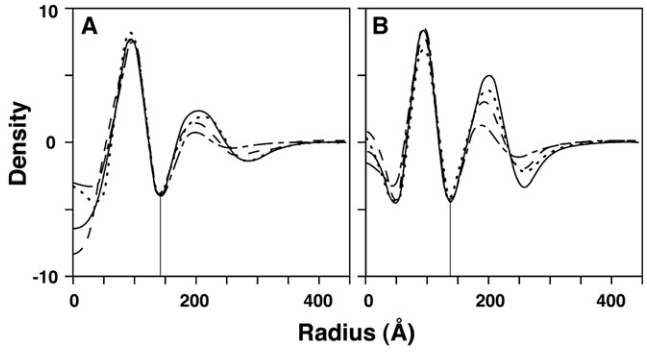

Figure 6. Density Distribution of Rotationally Averaged PDH Subcomplexes

Radial plots of densities derived from cryo-electron microscopic images of (A) E1E2 and (B) E2E3 subcomplexes are shown. The vertical lines highlight the dip in density at the position corresponding to the annular space between the E2 inner core and the outer E1 and E3 components. E2 cores decorated with 60, 40, 20, or 10 peripheral subunits are represented by (—), (· · · ·), (– –), or (– - –), respectively.

Using tomograms such as the ones shown in Figure 7, we obtained measurements of the distances between the inner core and each of the densities present on the periphery of the subcomplex. These measurements were then used to construct a histogram of individual distances observed in high- and low-occupancy subcomplexes (Figure 8). The height of the histogram

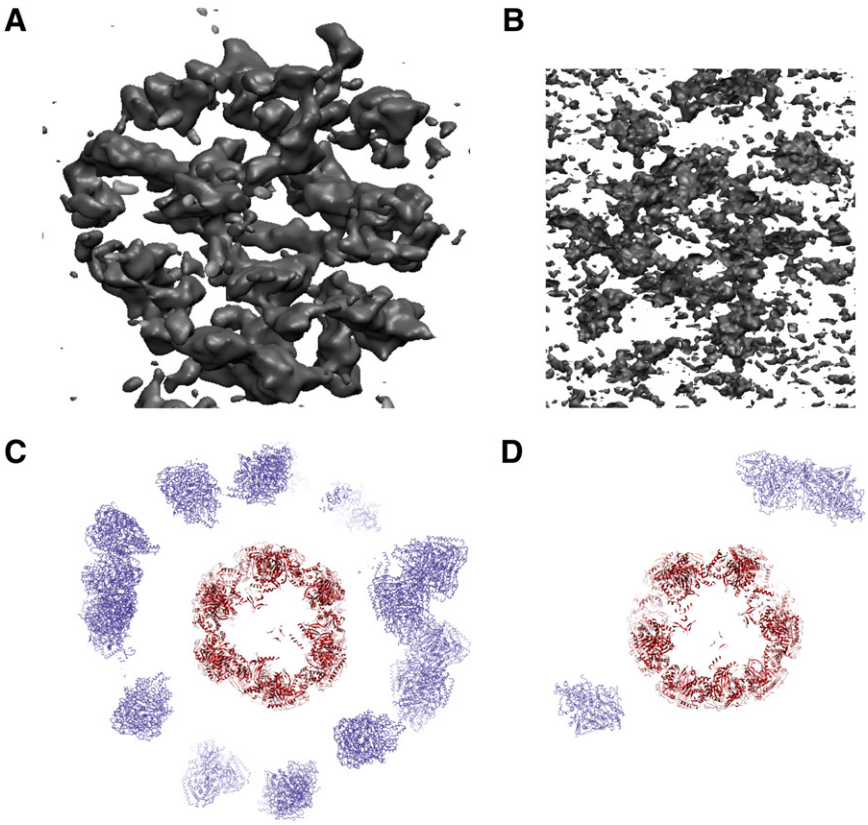

Figure 7. Cryo-Electron Tomgraphy of Single E1E2 Subcomplexes

Density maps of high (A) and low (B) occupancy E1E2 subcomplexes. (C and D) Atomic interpretations of central slices through the density maps shown in (A) and (B), respectively. The E2 inner core (red) and E1 heterotetramers (blue) were located with an automated core-weighted fitting algorithm as described in Experimental Procedures. The figures were generated by using VMD (Humphrey et al., 1996).

at any particular radial distance is therefore a statistically significant representation of the probability of finding an E1 molecule at that position. In the case of the full-occupancy subcomplexes, the highest probability of observing E1 molecules was at distances of ~220 Å from the center of the complex, in agreement with their positioning in the E1E2 subcomplex determined by means of single particle electron microscopy (Milne et al., 2002). Remarkably, a histogram obtained from analyses of low occupancy E1E2 subcomplexes with individual E1 occupancies ranging from 10%–20% shows a radial profile strikingly similar to that of the full-occupancy subcomplexes. These results conclusively demonstrate that the average radial distance of the outer shell enzymes from the E2 core in PDH complexes is determined primarily by the properties of the inner-linker region and not by clustering or interactions of neighboring E1 or E3 enzymes bound to the PSBD.

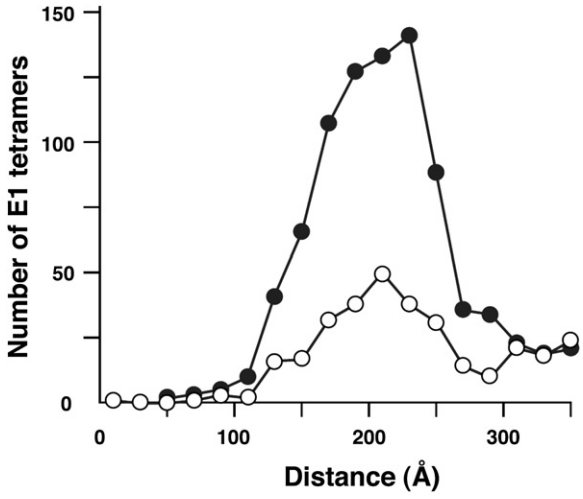

Figure 8. Distribution of E1 Components Relative to the E2 Core Derived by Molecular Fitting

Plot of the distance, measured from the center of the E2 core to the center of mass of each E1 heterotetramer on the periphery determined from 15 tomograms of high (black circles)- or low (open circles)-occupancy E1E2 subcomplexes.

DISCUSSION

Our results indicate that the inner-linker regions between the acetyltransferase core domains and PSBDs in the E2 core, which comprise less than 2% of the mass (~10 MDa) of the native *B. stearothermophilus* PDH complex, are not simply tethers that hold the constituent enzymes together in the complex. Circular dichroism, analytical ultracentrifugation, and NMR studies of a synthetic peptide representing the inner linker all consistently show that it adopts an extended, yet flexible, conformation. Analysis of projection and tomographic images of E1E2 and E2E3 subcomplexes at varying stages of assembly also demonstrate that the linker is extended in the context of the PDH complex. Even in cases with very low occupancy of peripheral E1 and E3 subunits, where the absence of clustered enzymes in the outer shell could be confirmed by visual inspection, the spacing between the inner core and the peripheral enzymes was similar to that seen in higher occupancy complexes. This rules out protein-protein interactions in the outer shell as being causative in the generation of the annular gap. While a high density of outer shell enzymes may prevent significant decreases in size of the overall complex by virtue of steric packing constraints, we conclude that it is the extension of the inner linker itself that is the primary determinant of the 75–90 Å annular gap in these multienzyme complexes.

Linkers that separate domains within a polypeptide chain are widespread and can vary greatly in their overall secondary structure and length, typically ~5–25 amino acids. Coiled-coil, α-helical, β sheet, and turn motifs are highly represented in linker regions, although a significant proportion of them appear to be

largely unstructured (George and Heringa, 2002; Wriggers et al., 2005). The inner linkers in the PDH family of complexes are among the longest known linker regions, and the results described here show that they play a critical dual role: holding the constituent enzymes of the complex together while spatially separating the inner catalytic E2 core from an outer shell of E1 and E3 components. The finding that a synthetic peptide corresponding to the linker region extending from Ala167 and Ser203 is relatively unstructured (Figure 2) is consistent with a predicted lack of secondary structure in this region (Milne et al., 2006) of the *B. stearothermophilus* E2. Based on the evidence that the peptide is monomeric in solution (Figure 3), and that its sequence (not least the Ala/Pro-rich N-terminal half) lacks the repeats of glycine residues that are required for triple helix formation, we conclude that the linker regions are unlikely to form higher order assemblies such as those found in collagen (Brodsky and Shah, 1995) and in the large Mda erythrocruorin complexes (Royer et al., 2007). In addition, the linkers as they emerge from adjacent acetyltransferase domains in the trimers at each of the 20 vertices of the E2 core are separated by ~42 Å, thus making close interactions between neighboring linkers unlikely (Milne et al., 2006).

The predicted persistence length of a random sequence 37 residue peptide, assuming a random walk model and a step size of 3.8 Å is 21.3 Å (Boal, 2002); this is far shorter then the length assumed by the actual peptide that can be estimated from analytical ultracentrifugation and the size of the annular gap as measured by electron microscopy. It is not entirely clear what unique features of the linker make it possible for the peptide to adopt an extended, yet relatively unstructured, conformation. The NMR analysis of the peptide presented in Figure 2 indicates that the proline residues of the inner *B. stearothermophilus* linker are primarily in the all-*trans* conformation, which is expected both to enhance elongation of the peptide and provide some degree of rigidity to it. Similar conclusions were reached in earlier NMR analyses of synthetic peptides representing the outer-linker regions that lie between the three lipoyl domains and the PSBD in the somewhat more complicated E2 chain of the PDH complex of *E. coli* (Radford et al., 1989; Green et al., 1992). In this case, however, the function of the linker region is clearly somewhat different, namely, to act as a highly flexible linker to permit a tethered lipoyl domain to migrate between widely separated E1, E2, and E3 active sites as part of the mechanism of active site coupling.

While it is to be expected that the properties of the linker in the context of the intact E2 polypeptide may be a little different from those of the synthetic peptide studied here, patterns in the secondary structure are likely to be conserved. Moreover, there is some earlier evidence from NMR spectroscopy that the inner-linker region (or at least the Ala-Pro-rich N-terminal part of it) enjoys significant conformational mobility in the corresponding (albeit octahedral) PDH and 2-oxoglutarate dehydrogenase complexes of *E. coli* (Radford et al., 1987). If this region of the E2p and E2o polypeptide chains, which links the E3-binding domain to the inner core-forming catalytic domain, does enjoy some degree of conformational freedom in the intact complexes, it would provide a structural basis for interpreting fluorescence data that suggest that E3 bound to the PDH complex is quite mobile (Grande et al., 1980).

Thus, we conclude that the inner-linker region is extended by virtue of its intrinsic properties and not because it is held in place between the catalytic E2 core and a well-packed outer shell of E1 and E3 components some 90 Å away. Given its length of ~37 amino acid residues and the size of the gap to be spanned between the E2 inner core and PSBD, the linker region can cross the gap only once. No density corresponding to any part of this region is evident in 3D reconstructions of E1E2 (Milne et al., 2002) or E2E3 (Milne et al., 2006) subcomplexes. Irrespective of how the extended structure arises, the linker must have a bending modulus that is adequate to allow small variations in shape, without large excursions from the average extended conformation.

The relatively high population (20%) of a type-VI turn in the synthetic peptide is due to the presence of an aromatic residue (Phe) in the position preceding Pro30 and ring-stacking stabilization effects (Yao et al., 1994), and thus the turn is expected to be present at around the 20% level in all inner linkers. An alignment of E2 chains from several organisms (carried out with EMBL-EBI alignment tools, data not shown) reveals that the sequence necessary to form a type-VI turn is conserved among several PDH complexes (FP or YP being the residues required for formation of the type-VI turn). The type-VI turn at this position was seen in the X-ray crystal structures of the octahedral inner core of the *Azotobacter vinelandii* PDH complex (Mattevi et al., 1992) and the icosahedral inner core of the *B. stearothermophilus* PDH complex (Izard et al., 1999). Further, single particle reconstruction of the *B. stearothermophilus* E2 core in which the C-terminal portion of the inner-linker region was retained revealed a density consistent with the shape and position of the type-VI turn that was transiently populated at ~10% frequency in solution (Rosenthal and Henderson, 2003). The significance of this alternative, albeit infrequently populated, conformation is not yet clear, although it may allow occasional excursions of the outer shell enzymes toward the E2 core.

Visualization of the dynamic nature of the peripheral E1 and E3 subunits is not possible from single-particle averaging experiments (Milne et al., 2002, 2006) but emerges clearly from our cryo-tomographic anlaysis of E1E2 complexes, which show that the arrangement of outer shell enzymes can deviate from perfect icosahedral symmetry by lateral movements within the outer shell layer, as previously suggested (Milne et al., 2002, 2006), as well as by movements toward the core. These movements must depend upon the intrinsic conformational flexibility of the linker, which may involve rotational movements to permit lateral movement of the peripheral subunits or flicking into type-VI turn mode to move these enzymes transiently closer to the core. Since it is not possible to visualize directly the density of the linkers by cryo-electron microscopy, it is also possible that positioning of E1 enzymes close to a particular E2 subunit could sometimes arise from linkers which originate from adjacent E2 subunits that are farther away. In this event, such linkers could be as fully extended as in the cases where the E1 enzymes are at their maximal radial extension.

There is clear evidence that the two E1 active sites within the $\alpha_2\beta_2$ tetramer act alternately during sequential catalytic cycles (Frank et al., 2004, 2005; Seifert et al., 2006). Our model for the architecture of the PDH complex would enable both active sites of E1 to be accessible to lipoyl domains within the gap. This type of conformational heterogeneity allows the lipoyl domains exiting the E2 active sites after delivering their cargo of acetyl groups to

make efficacious contact with the far fewer E3 molecules compared with E1 in a native PDH complex (Perham, 2000). Thus, the ability of the inner linker to be extended and yet flexible provides an elegant means of increasing the efficiency of active site coupling by generating an annular space in which to increase the local concentration of lipoyl domains while enhancing their interactions with both peripheral (E1 and E3) enzymes.

Almost every aspect of the architecture of PDH complexes appears to have become optimized in a way to provide the type of flexibility needed to execute the complicated series of reactions that is required for the oxidative decarboxylation of pyruvate and formation of acetyl CoA. In our previous studies, we deduced that there must be flexibility in the arrangement of the E1 and E3 enzymes along the surface of the outer shell based on analysis of fully assembled E1E2 and E2E3 subcomplexes (Milne et al., 2002, 2006). The structural analysis of the linker region presented here highlights the potential for some flexibility in radial positioning of the E1 and E3 complexes in native complexes. This remarkable combination of a well-defined E2 core scaffold that serves as the foundation for assembly of the flexible concatenation of linked E2 domains and peripheral E1/E3 components is the distinctive hallmark of the PDH multienzyme complexes.

EXPERIMENTAL PROCEDURES

Inner-Linker Peptide Synthesis and Purification

A peptide with the sequence AGGAKPAPAAAEEKAAPAAAKPATTEGEFPET REKMS was synthesized by the solid-phase method with Fmoc (9-fluorenylmethoxycarbonyl) chemistry on a model 431A peptide synthesizer (Applied Biosystems, Foster City, CA, USA). The peptide was cleaved with 82.5% trifluoroacetic acid (TFA)/5% phenol/5% thioanisole/5% water/2.5% ethandithiol and then purified by reversed-phase high-performance liquid chromatography (RP-HPLC) on a Vydac C-4 column with 0.05% TFA/water/acetonitrile. The purity of the peptide was >95% as determined by analytical RP-HPLC, and its mass was 3638.6 Da (predicted mass 3640.0 Da) as measured by matrix-assisted laser desorption ionization time-of-flight mass spectrometry (Micromass, Beverly, MA).

Circular Dichroism Spectroscopy

Background corrected circular dichroism spectra were collected on a Jobin-Yvon CD6 circular dichrograph at 25°C in 1.0 mm cuvettes (Starna, Optiglass, Ltd.). One millimolar peptide samples were prepared in 10 mM potassium phosphate buffer (PB; pH 7.0). The spectra were collected between 185 nm and 260 nm in 1 nm intervals. The data was expressed as molar ellipticity ([θ], deg cm^2/dmol).

Analytical Ultracentrifugation

Sedimentation velocity experiments were conducted with an Optima XLI/A (Beckman Coulter, Fullerton, CA, USA). After exhaustive dialysis of the peptide against 20 mM PB, 20 mM NaCl (pH 7.0), samples (400 μl) were loaded at concentrations of 0.8 and 0.27 mg/ml and centrifuged at 60,000 rpm at 19°C. Sedimentation data were acquired with the Rayleigh interference optical system and simultaneously with the absorbance optical system at a wavelength of 240 nm. Data analysis was performed with the software SEDPHAT (http://www.analyticalultracentrifugation.com/sedphat/sedphat.htm) by globally fitting the data acquired at different detection systems and loading concentrations, by using a single ideal Lamm equation solution (Schuck, 1998) to describe the entire time course of sedimentation, with the radial range including significant back diffusion. Best fits were found with random residuals consistent with the noise of data acquisition (average root-mean-square deviation ~0.006 fringes and <0.005 OD), generating a best-fit molecular mass of 3.62 kDa, close to the theoretically expected value of 3.64 kDa. Separate analyses of the absorbance and interference data did not show any significant systematic variation, indicating the absence of signal contributions from residual unmatched buffer components. No evidence of additional sedimenting species was obtained in the c(s) method. Error estimates of the sedimentation coefficients (~0.002S) were derived from projection of the error surface by F statistics and independently from the variation of results of individual fits to replicate experiments. Hydration estimates based on amino acid composition by the method of Kuntz (1971), the peptide partial specific volume, and the dimensions of the hydrodynamically equivalent ellipsoid were computed with the software package SEDNTERP (http://www.rasmb.bbri.org/).

NMR Spectroscopy

NMR measurements were made at 500 MHz on proteins (1 mM) in 10% D_2O in 10 mM PB (pH 7.0) at 25°C. Chemical-shift assignments were derived from established versions of 2D NOESY (200 ms mixing time), TOCSY (69 ms mixing time), and ^1H-^{13}C-HSQC experiments (Cavanagh et al., 1996) and internally referenced to DSS. In all experiments, water suppression was achieved by established flip-back methods to return the water magnetization to the z axis and WATERGATE (Sklenar et al., 1993). Data were processed with the AZARA suite of programs (v. 2.7, copyright 1993–2002, Wayne Boucher and Department of Biochemistry, University of Cambridge). Assignments were made with Analysis v. 1.0 (Vranken et al., 2005) (copyright 2004 Wayne Boucher and Tim Stevens, University of Cambridge). Deviations from random-coil chemical shifts (Schwarzinger et al., 2000) were corrected for sequence-dependent effects (Schwarzinger et al., 2001) with the exception of Glu residues, for which the random-coil shifts were taken from a consensus of data from unstructured peptides at neutral pH reported in the BioMagResBank (Seavey et al., 1991). This circumvents large systematic errors that arise due to the use of strongly acidic conditions in the original study.

PDH Complex Preparation

The E1, E2, and E3 components of the *B. stearothermophilus* PDH complex were purified as recombinant protein products from genes expressed in *E. coli* as described (Lessard and Perham, 1994; Lessard et al., 1998) to final concentrations of 10 mg/ml, 2 mg/ml, and 6 mg/ml, respectively, in 50 mM PB, 150 mM NaCl (pH 7.0). Components were reconstituted (2 hr, 25°C) to generate E1E2 and E2E3 subcomplexes, which were separated from unbound E1 or E3 by using CL-2B Sepharose size-exclusion chromatography in the same buffer containing 0.02% (w/v) sodium azide (Lessard et al., 1998; Domingo et al., 1999). Fractions containing E1E2 or E2E3 subcomplexes were pooled, concentrated with a Vivaspin 100 kDa concentrator (3,500 rpm at 4°C), and snap frozen for storage at −80°C. Complexes were generated with E1:E2 and E3:E2 polypeptide chain ratios of 10:60, 20:60, 40:60, and 60:60 corresponding to E1 or E3 occupancy levels of 17%, 33%, 67%, and 100%, respectively. The chain ratio of each complex was confirmed by electrophoresis on 10% Bis-Tris NUPAGE gels, stained with Blue Code (Pierce), and analyzed by densitometry.

Electron Microscopy and Image Processing

Untilted images of frozen-hydrated specimens of each subcomplex were digitally recorded at 52,000× magnification by using electron doses of ~10 $e^-/Å^2$ on a FEI Tecnai 12 microscope operating at liquid nitrogen temperatures equipped with a 4 k × 4 k CCD camera (Gatan, Inc.). Images were recorded at an underfocus of ~2.63 μm, with an image pixel size corresponding to 2.13 Å on the specimen plane. Well-separated individual complexes were selected by using the MRC display program Ximdisp (Smith, 1999) with a box size of 384 × 384 pixels. Rotational averages were generated with the IMAGIC image processing package (van Heel et al., 1996). Images were filtered to retain information over spatial frequencies between 100–30 Å and iteratively aligned translationally against a rotational average of all nonaligned images.

Cryo-Electron Tomography

Tilts series were collected over a range of −65° to +65° in 3° steps by using an FEI Polara (FEI) microscope operating at 300 kV equipped with a Gatan energy filter using a 30 eV slit width under low-dose conditions at cryogenic temperatures. Images were collected at the nominal magnification of 34,000× (0.58 nm/pixel) with underfocus values of ~5 μm. The total dose per tilt series was <60 $e^-/Å^2$, distributed linearly over the course of the tilt series. Tilt series were aligned and reconstructed with Inspect 3D (FEI) software implementing the SIRT reconstruction procedure.

Positioning Atomic Coordinates into Tomographic Densities

Placement of the coordinates for the E2 core, E1 heterotetramer, and the E3 dimer from *B. stearothermophilus* (Protein Data Bank entries 1B5S, 1W85, and 1EBD, respectively) was performed by using a core-weighted Monte Carlo grid-searching algorithm (Wu et al., 2003). Briefly, the C^{α} coordinates of the E1 heterotetramer associated with PSBD, the E3 dimer associated with PSBD, or the icosahedral core of E2 generated by application of icosahedral symmetry matrices to the E2 catalytic subunit were used to generate a density map of 30 Å resolution with the Gaussian blurring procedure implemented in CHARMM (version 32). A grid-threading Monte Carlo method was used to search the six-dimensional translational and rotational space of the densities of each of the E1E2 or E2E3 complexes. The translational space was divided into a 3 × 3 × 3 grid, and at each translational grid point, the orientational space was divided into a 3 × 3 × 3 grid, which was then used to initiate 1000-step MC searches to identify local maximums of the core-weighted correlated function from which the final global maximum was identified. To facilitate analysis, the E2 core was first positioned into the tomographic density prior to analysis of the E1 heterotetramers or the E3 dimers, respectively.

ACKNOWLEDGMENTS

We thank Ettore Appella (Laboratory of Cell Biology, National Cancer Institute, Bethesda) for synthesis of the inner-linker peptide and John Philo (Alliance Protein Laboratories) for providing SEDNTERP. J.S.L. is a scholar in the National Institutes of Health-Cambridge Graduate Partnership Program. This work was supported by intramural funding from the Center for Cancer Research, National Cancer Institute, National Institutes of Health to J.L.S.M. and S.S.

Received: March 27, 2007
Revised: October 15, 2007
Accepted: October 17, 2007
Published: January 8, 2008

REFERENCES

Allen, M.D., Broadhurst, R.W., Solomon, R.G., and Perham, R.N. (2005). Interaction of the E2 and E3 components of the pyruvate dehydrogenase multienzyme complex of *Bacillus stearothermophilus*. Use of a truncated protein domain in NMR spectroscopy. FEBS J. *272*, 259–268.

Arjunan, P., Nemeria, N., Brunskill, A., Chandrasekhar, K., Sax, M., Yan, Y., Jordan, F., Guest, J.R., and Furey, W. (2002). Structure of the pyruvate dehydrogenase multienzyme complex E1 component from *Escherichia coli* at 1.85 Å resolution. Biochemistry *41*, 5213–5221.

Boal, D. (2002). Mechanics of the Cell (Cambridge, United Kingdom: Cambridge University Press).

Brodsky, B., and Shah, N.K. (1995). Protein motifs. 8. The triple-helix motif in proteins. FASEB J. *9*, 1537–1546.

Bubber, P., Haroutunian, V., Fisch, G., Blass, J.P., and Gibson, G.E. (2005). Mitochondrial abnormalities in Alzheimer brain: mechanistic implications. Ann. Neurol. *57*, 695–703.

Cavanagh, J., Fairbrother, W.J., Palmer, A.G., and Skelton, N.J. (1996). Protein NMR Spectroscopy: Principles and Practice (San Diego: Academic Press).

Ciszak, E.M., Makal, A., Hong, Y.S., Vettaikkorumakankauv, A.K., Korotchkina, L.G., and Patel, M.S. (2006). How dihydrolipoamide dehydrogenase-binding protein binds dihydrolipoamide dehydrogenase in the human pyruvate dehydrogenase complex. J. Biol. Chem. *281*, 648–655.

Dardel, F., Davis, A.L., Laue, E.D., and Perham, R.N. (1993). Three-dimensional structure of the lipoyl domain from *Bacillus stearothermophilus* pyruvate dehydrogenase multienzyme complex. J. Mol. Biol. *229*, 1037–1048.

Domingo, G.J., Chauhan, H.J., Lessard, I.A.D., Fuller, C., and Perham, R.N. (1999). Self-assembly and catalytic activity of the pyruvate dehydrogenase multienzyme complex from *Bacillus stearothermophilus*. Eur. J. Biochem. *266*, 1136–1146.

Frank, R.A., Titman, C.M., Pratap, J.V., Luisi, B.F., and Perham, R.N. (2004). A molecular switch and proton wire synchronize the active sites in thiamine enzymes. Science *306*, 872–876.

Frank, R.A., Pratap, J.V., Pei, X.Y., Perham, R.N., and Luisi, B.F. (2005). The molecular origins of specificity in the assembly of a multienzyme complex. Structure *13*, 1119–1130.

Fries, M., Stott, K.M., Reynolds, S., and Perham, R.N. (2007). Distinct modes of recognition of the lipoyl domain as substrate by the E1 and E3 components of the pyruvate dehydrogenase multienzyme complex. J. Mol. Biol. *366*, 132–139.

George, R.A., and Heringa, J. (2002). An analysis of protein domain linkers: their classification and role in protein folding. Protein Eng. *15*, 871–879.

Grande, H.J., Visser, A.J., and Veeger, C. (1980). Protein mobility inside pyruvate dehydrogenase complexes as reflected by laser-pulse fluorometry. A new approach to multi-enzyme catalysis. Eur. J. Biochem. *106*, 361–369.

Green, J.D.F., Perham, R.N., Ullrich, S.J., and Appella, E. (1992). Conformational studies of the interdomain linker peptides in the dihydrolipoyl acetyltransferase component of the pyruvate dehydrogenase multienzyme complex of *Escherichia coli*. J. Biol. Chem. *267*, 23484–23488.

Gu, Y., Zhou, Z.H., McCarthy, D.B., Reed, L.J., and Stoops, J.K. (2003). 3D electron microscopy reveals the variable deposition and protein dynamics of the peripheral pyruvate dehydrogenase component about the core. Proc. Natl. Acad. Sci. USA *100*, 7015–7020.

Humphrey, W., Dalke, A., and Schulten, K. (1996). VMD: visual molecular dynamics. J. Mol. Graph. *14*, 33–38.

Izard, T., Ævarsson, A., Allen, M.D., Westphal, A.H., Perham, R.N., de Kok, A., and Hol, W.G.J. (1999). Principles of quasi-equivalence and Euclidean geometry govern the assembly of cubic and dodecahedral cores of pyruvate dehydrogenase complexes. Proc. Natl. Acad. Sci. USA *96*, 1240–1245.

Kale, S., Arjunan, P., Furey, W., and Jordan, F. (2007). A dynamic loop at the active center of the *Escherichia coli* pyruvate dehydrogenase complex E1 component modulates substrate utilization and chemical communication with the E2 component. J. Biol. Chem. *282*, 28106–28116.

Kalia, Y.N., Brocklehurst, S.M., Hipps, D.S., Appella, E., Sakaguchi, K., and Perham, R.N. (1993). The high resolution structure of the peripheral subunit-binding domain of dihydrolipoamide acetyltransferase from the pyruvate dehydrogenase multienzyme complex of *Bacillus stearothermophilus*. J. Mol. Biol. *230*, 323–341.

Kim, J.W., Tchernyshyov, I., Semenza, G.L., and Dang, C.V. (2006). HIF-1-mediated expression of pyruvate dehydrogenase kinase: a metabolic switch required for cellular adaptation to hypoxia. Cell Metab. *3*, 177–185.

Koukourakis, M.I., Giatromanolaki, A., Sivridis, E., Gatter, K.C., and Harris, A.L. (2005). Pyruvate dehydrogenase and pyruvate dehydrogenase kinase expression in non small cell lung cancer and tumor-associated stroma. Neoplasia *7*, 1–6.

Kuntz, I.D. (1971). Hydration of macromolecules. III. Hydration of polypeptides. J. Am. Chem. Soc. *93*, 514–516.

Lessard, I.A.D., and Perham, R.N. (1994). Expression in *Escherichia coli* of genes encoding the Elα and E1β subunits of the pyruvate dehydrogenase complex of *Bacillus stearothermophilus* and assembly of a functional El component ($\alpha_2\beta_2$) in vitro. J. Biol. Chem. *269*, 10378–10383.

Lessard, I.A.D., and Perham, R.N. (1995). Interaction of component enzymes with the peripheral subunit-binding domain of the pyruvate dehydrogenase multienzyme complex from *Bacillus stearothermophilus*: stoichiometry and specificity in self assembly. Biochem. J. *306*, 727–733.

Lessard, I.A.D., Domingo, G.J., Borges, A., and Perham, R.N. (1998). Expression of genes encoding the E2 and E3 components of the *Bacillus stearothermophilus* pyruvate dehydrogenase complex and the stoichiometry of subunit interaction in assembly in vitro. Eur. J. Biochem. *258*, 491–501.

Mande, S.S., Sarfaty, S., Allen, M.D., Perham, R.N., and Hol, W.G.J. (1996). Protein-protein interactions in the pyruvate dehydrogenase multienzyme complex: dihydrolipoamide dehydrogenase complexed with the binding domain of dihydrolipoamide acetyltransferase. Structure *4*, 277–286.

Mattevi, A., Obmolova, G., Schulze, E., Kalk, K.H., Westphal, A.H., de Kok, A., and Hol, W.G.J. (1992). Atomic structure of the cubic core of the pyruvate dehydrogenase multienzyme complex. Science *255*, 1544–1550.

Milne, J.L.S., Shi, D., Rosenthal, P.B., Sunshine, J.S., Domingo, G.J., Wu, X., Brooks, B.R., Perham, R.N., Henderson, R., and Subramaniam, S. (2002). Molecular architecture and mechanism of an icosahedral pyruvate dehydrogenase complex: a multifunctional catalytic machine. EMBO J. *21*, 5587–5598.

Milne, J.L.S., Wu, X., Borgnia, M.J., Lengyel, J.S., Brooks, B.R., Shi, D., Perham, R.N., and Subramaniam, S. (2006). Molecular structure of a 9 MDa icosahedral pyruvate dehydrogenase sub-complex containing the E2 and E3 enzymes using cryo-electron microscopy. J. Biol. Chem. *281*, 4364–4370.

Murphy, G.E., and Jensen, G.J. (2005). Electron cryotomography of the *E. coli* pyruvate and 2-oxoglutarate dehydrogenase complexes. Structure *13*, 1765–1773.

Nellis, M.M., and Danner, D.J. (2001). Gene preferences in maple syrup urine disease. Am. J. Hum. Genet. *68*, 232–237.

Patel, M.S., and Harris, R.A. (1995). Mammalian α-keto acid dehydrogenase complexes—gene regulation and genetic defects. FASEB J. *9*, 1164–1172.

Perham, R.N. (1991). Domains, motifs, and linkers in 2-oxo acid dehydrogenase multienzyme complexes: a paradigm in the design of a multifunctional protein. Biochemistry *30*, 8501–8512.

Perham, R.N. (2000). Swinging arms and swinging domains in multifunctional enzymes: catalytic machines for multistep reactions. Annu. Rev. Biochem. *69*, 961–1004.

Radford, S.E., Laue, E.D., Perham, R.N., Miles, J.S., and Guest, J.R. (1987). Segmental structure and protein domains in the pyruvate dehydrogenase multienzyme complex of *Escherichia coli*. Genetic reconstruction in vitro and ^{1}H-n.m.r. spectroscopy. Biochem. J. *247*, 641–649.

Radford, S.E., Laue, E.D., Perham, R.N., Martin, S.R., and Appella, E. (1989). Conformational flexibility and folding of synthetic peptides representing an interdomain segment of polypeptide chain in the pyruvate dehydrogenase multienzyme complex of *Escherichia coli*. J. Biol. Chem. *264*, 767–775.

Reed, L.J., and Hackert, M.L. (1990). Structure-function relationships in dihydrolipoamide acyltransferases. J. Biol. Chem. *265*, 8971–8974.

Rosenthal, P.B., and Henderson, R. (2003). Optimal determination of particle orientation, absolute hand, and contrast loss in single-particle electron cryomicroscopy. J. Mol. Biol. *333*, 721–745.

Royer, W.E., Jr., Omartian, M.N., and Knapp, J.E. (2007). Low resolution crystal structure of *Arenicola* erythrocruorin: influence of coiled coils on the architecture of a megadalton respiratory protein. J. Mol. Biol. *365*, 226–236.

Schuck, P. (1998). Sedimentation analysis of noninteracting and self-associating solutes using numerical solutions to the Lamm equation. Biophys. J. *75*, 1503–1512.

Schwarzinger, S., Kroon, G.J., Foss, T.R., Wright, P.E., and Dyson, H.J. (2000). Random coil chemical shifts in acidic 8 M urea: implementation of random coil shift data in NMRView. J. Biomol. NMR *18*, 43–48.

Schwarzinger, S., Kroon, G.J., Foss, T.R., Chung, J., Wright, P.E., and Dyson, H.J. (2001). Sequence-dependent correction of random coil NMR chemical shifts. J. Am. Chem. Soc. *123*, 2970–2978.

Seavey, B.R., Farr, E.A., Westler, W.M., and Markley, J.L. (1991). A relational database for sequence-specific protein NMR data. J. Biomol. NMR *1*, 217–236.

Seifert, F., Golbik, R., Brauer, J., Lilie, H., Schroder-Tittmann, K., Hinze, E., Korotchkina, L.G., Patel, M.S., and Tittmann, K. (2006). Direct kinetic evidence for half-of-the-sites reactivity in the E1 component of the human pyruvate dehydrogenase multienzyme complex through alternating sites cofactor activation. Biochemistry *45*, 12775–12785.

Sklenar, V., Piotto, M., Leppik, R., and Saudek, V. (1993). Gradient-tailored water suppression for ^{1}H ^{15}N HSQC experiments optimized to retain full sensitivity. J. Magn. Reson. A *102*, 241–245.

Smith, J.M. (1999). Ximdisp—a visualization tool to aid structure determination from electron microscope images. J. Struct. Biol. *125*, 223–228.

Tahara, E.B., Barros, M.H., Oliveira, G.A., Netto, L.E.S., and Kowaltowski, A.J. (2007). Dihydrolipoyl dehydrogenase as a source of reactive oxygen species inhibited by caloric restriction and involved in *Saccharomyces cerevisiae* aging. FASEB J. *21*, 274–283.

van Heel, M., Harauz, G., Orlova, E.V., Schmidt, R., and Schatz, M. (1996). A new generation of the IMAGIC image processing system. J. Struct. Biol. *116*, 17–24.

Vranken, W.F., Boucher, W., Stevens, T.J., Fogh, R.H., Pajon, A., Llinas, M., Ulrich, E.L., Markley, J.L., Ionides, J., and Laue, E.D. (2005). The CCPN data model for NMR spectroscopy: development of a software pipeline. Proteins *59*, 687–696.

Wagenknecht, T., Grassucci, R., and Schaak, D. (1990). Cryoelectron microscopy of frozen-hydrated α-ketoacid dehydrogenase complexes from *Escherichia coli*. J. Biol. Chem. *265*, 22402–22408.

Wagenknecht, T., Grassucci, R., Radke, G.A., and Roche, T.E. (1991). Cryoelectron microscopy of mammalian pyruvate dehydrogenase complex. J. Biol. Chem. *266*, 24650–24656.

Wagenknecht, T., Grassucci, R., Berkowitz, J., and Forneris, C. (1992). Configuration of interdomain linkers in pyruvate dehydrogenase complex of *Escherichia coli* as determined by cryoelectron microscopy. J. Struct. Biol. *109*, 70–77.

Wishart, D.S., Sykes, B.D., and Richards, F.M. (1991). Relationship between nuclear magnetic resonance chemical shift and protein secondary structure. J. Mol. Biol. *222*, 311–333.

Wishart, D.S., Bigam, C.G., Holm, A., Hodges, R.S., and Sykes, B.D. (1995). ^{1}H, ^{13}C and ^{15}N random coil NMR chemical shifts of the common amino acids. I. Investigations of nearest-neighbor effects. J. Biomol. NMR *5*, 67–81.

Wriggers, W., Chakravarty, S., and Jennings, P.A. (2005). Control of protein functional dynamics by peptide linkers. Biopolymers *80*, 736–746.

Wu, X., Milne, J.L.S., Borgnia, M.J., Rostapshov, A.V., Subramaniam, S., and Brooks, B.R. (2003). A core-weighted fitting method for docking atomic structures into low-resolution maps: application to cryo-electron microscopy. J. Struct. Biol. *141*, 63–76.

Wüthrich, K. (1986). NMR of Proteins and Nucleic Acids (New York: John Wiley & Sons).

Yao, J., Feher, V.A., Espejo, B.F., Reymond, M.T., Wright, P.E., and Dyson, H.J. (1994). Stabilization of a type VI turn in a family of linear peptides in water solution. J. Mol. Biol. *243*, 736–753.

Yeaman, S.J., Kirby, J.A., and Jones, D.E.J. (2000). Autoreactive responses to pyruvate dehydrogenase complex in the pathogenesis of primary biliary cirrhosis. Immunol. Rev. *174*, 238–249.

Zhou, Z.H., McCarthy, D.B., O'Connor, C.M., Reed, L.J., and Stoops, J.K. (2001). The remarkable structural and functional organization of the eukaryotic pyruvate dehydrogenase complexes. Proc. Natl. Acad. Sci. USA *98*, 14802–14807.

Accession Numbers

Chemical-shift assignments for the inner-linker peptide have been deposited with the BioMagResBank under the accession number 15612.